Atmos. Meas. Tech. Discuss., doi:10.5194/amt-2016-268, 2016
Manuscript under review for journal Atmos. Meas. Tech.
Published: 7 September 2016

Atmospheric Measurement Techniques
Discussions
Open Access

Deriving clear-sky longwave spectral flux solely from hyperspectral radiance: a case study with AIRS observations

Xiuhong Chen*, Xianglei Huang

Department of Climate and Space Sciences and Engineering, the University of Michigan at Ann Arbor.

* Corresponding author: Dr. Xiuhong Chen, Department of Climate and Space Sciences and Engineering, the University of Michigan, Ann Arbor, MI 48109-2143, USA. (Tel) 734-647-7687.

xiuchen@umich.edu

Atmos. Meas. Tech. Discuss., doi:10.5194/amt-2016-268, 2016
Manuscript under review for journal Atmos. Meas. Tech.
Published: 7 September 2016

Atmospheric Measurement Techniques Discussions
Open Access

Abstract

Previous studies have shown that longwave (LW) spectral fluxes have unique merit in climate studies. Using Atmospheric Infrared Sounder (AIRS) radiances as a case study, this study presents an algorithm to derive the entire LW clear-sky spectral fluxes solely from hyperspectral observations. No other auxiliary observations are needed in the algorithm. A clear-sky scene is identified using a three-step detection method. The identified clear-sky scenes are then categorized into different sub-scene types using AIRS radiances at six selected channels. A previously established algorithm is then used to invert AIRS radiances to spectral fluxes over the entire LW spectrum at 10 cm^{-1} spectral interval. Accuracy of the algorithms is evaluated against collocated Clouds and the Earth's Radiant Energy System (CERES) observations. For nadir-view observations, the mean difference between outgoing longwave radiation (OLR) derived by this algorithm and the collocated CERES OLR is 1.52 Wm^{-2} with a standard deviation of 2.46 Wm^{-2}. When the algorithm is extended for viewing zenith angle up to 45°, the performance is comparable to that for nadir-view results.

Key words: longwave spectral flux; OLR; clear-sky detection; sub-scene type classification; hyperspectral observations; AIRS

Atmos. Meas. Tech. Discuss., doi:10.5194/amt-2016-268, 2016
Manuscript under review for journal Atmos. Meas. Tech.
Published: 7 September 2016

Atmospheric Measurement Techniques Discussions

1. Introduction

Broadband outgoing longwave radiation (OLR) obtained by Earth's Radiation Energy Balance (ERBE; Barkstrom 1984) and Clouds and the Earth's Radiant Energy System (CERES; Wielicki et al., 1996) has been extensively used in climate studies for three decades. The physical quantity directly measured by the ERBE or CERES instruments is actually a convolution between broadband upwelling radiance at a given viewing zenith angle and the spectral response function (SRF) of the broadband radiometer on the EREB or CERES. Then the broadband upwelling radiance is inferred through deconvolution of the measurement and, consequently, it is converted to broadband flux (e.g. Loeb et al., 2005; Kato and Loeb, 2005). In order to reliably derive the broadband flux, a variety of auxiliary information needs to be used to define the scene type for each instrument footprint. Such auxiliary information includes, but is not limited to, surface temperature, lapse rate, precipitable water, and cloud macroscopic properties (e.g. cloud fraction, cloud emissivity). For the case of CERES, such auxiliary information is obtained from other satellite measurements such as MODIS and SSM/I as well as operational analysis (Loeb et al., 2005).

The integrand of broadband OLR, the spectral flux, is not available from the broadband flux measurements such as ERBE or CERES because of the nature of broadband radiometer in these measurements. However, the spectral flux can provide critically valuable information for the climate model diagnostics. Especially, comparing modeled and observed spectral flux can expose compensating biases in the simulated radiation budget by the climate model that otherwise cannot be exposed from broadband flux diagnostics alone (Huang et al., 2006; Huang et al., 2013; Huang et al., 2014). Similarly, spectral cloud radiative forcing can also help expose compensating biases from different bands (Huang et al., 2013; Huang et al., 2014).

Currently there are several operational hyperspectral sounders in space that measure spectral radiances in thousands of IR channels, for example, Atmospheric Infrared Sounder (AIRS; Aumann et al., 2003) since 2002, Infrared Atmospheric Sounding Interferometer (IASI; Hilton et al., 2012) since 2006, and Cross-track Infrared Sounder (CrIS; Han et al., 2013; Strow et al., 2013) since 2011. Each of these sounders can acquire several millions of spectra per day. A series of studies published in recent years (Huang et al., 2008, 2010, 2014; Chen et al., 2013) have established algorithms to estimate observation-based spectral flux from the AIRS radiances using the scene type information from collocated CERES footprints. Specifically, spectral angular distribution models (ADMs) for each AIRS channel have been constructed for the scene types defined for the CERES SSF (Single Satellite Footprint) data set and then applied to AIRS radiances to derive spectral flux at each AIRS channel. The spectral ADMs are trained from synthetic AIRS radiances and the meteorological fields from the ECMWF ERA-Interim reanalysis (Dee et al., 2011) that are used to generate the synthetic radiances. A principal component-based multivariate linear regression scheme is then used to estimate spectral flux over the spectral bands not covered by the AIRS instrument. The end product is spectral flux at 10 cm^{-1} interval over the entire LW spectrum. The spectral flux derived from this method has been extensively compared with collocated CERES OLR and the agreement is robustly consistent across different scene types and over different spatial and time scales, from footprint level to gridded data, from monthly means to annual means and interannual variations (Huang et al., 2008, 2010, 2014; Chen et al., 2013).

The aforementioned series of studies took a shortcut by relying on the scene type information from collocated CERES dataset. The other hyper-spectral sounders such as CrIS and IASI also fly with imagers such as VIIRS and AVHRR, respectively. These imagers provide information needed for scene type classification. However, to apply information from these imagers, the near-simultaneous observations as well as the collocation strategy are required to overcome the differences in observational area and time period (Huang et al., 2008; O'Carroll et al., 2012; Wang et al., 2013). The rich information contained in the hyperspectral radiances naturally leads to a hypothesis that all information needed for defining scene types might be already contained in the spectral radiances. Therefore, a scientifically intriguing question to ask is: can we directly estimate spectral flux from such observations of hyperspectral radiances without relying on auxiliary observations and thus avoid the trouble of collocation strategy and reduction of samples? To follow this line of thinking, this study explores ways of defining scene types and sub-scene types solely from hyperspectral measurements such as AIRS radiances, and then evaluates the spectral flux derived in this manner. As a first step, we focus on clear-sky scene types in this study. This effort aims to estimate longwave spectral flux and broadband OLR directly from AIRS Level-1 calibrated radiances over each individual single footprint. This approach is different from other studies such as Dessler et al. (2008), Moy et al. (2010) and Susskind et al. (2012), which fed temperature and humidity fields from AIRS Level-2 retrievals (defined for 3-by-3 AIRS footprints) or even Level-3 monthly gridded data set into a radiative transfer model to compute the clear-sky OLR. Huang et al. (2008, 2010, 2014) and Chen et al. (2013) have demonstrated that such direct estimate of spectral flux from AIRS radiances is feasible and the estimated OLR highly agree with the collocated CERES OLR. Furthermore, the

Atmos. Meas. Tech. Discuss., doi:10.5194/amt-2016-268, 2016
Manuscript under review for journal Atmos. Meas. Tech.
Published: 7 September 2016

merit of the spectral flux in testing climate models also warrants a feasibility study of deriving spectral flux (preferably over the entire longwave spectrum) from the hyperspectral satellite observations. All these facts have motivated the study presented in this article.

The rest of this paper is organized as follows. Section 2 describes the dataset and forward model used in this study. Clear-sky detection, sub-scene type classification, and the derivation of spectral flux for the case of nadir-view observations are described in Section 3. Section 4 validates the overall algorithm mentioned in Section 3. Section 5 discusses performances of the algorithm in other viewing zenith angles within ±45°. Conclusions and further discussion are then presented in Section 6.

2. Data sets and forward model

The data sets and forward model used in this study are identical to those used in (Huang et al., 2008; Chen et al., 2013). Below is a brief depiction of the relevant features of data and forward model.

AIRS is an infrared grating array spectrometer aboard NASA's Aqua satellite launched in 2002 (Aumann et al., 2003). It measures radiances across three bands, 3.74-4.61 μm, 6.20-8.22 μm and 8.8-15.4 μm, with a spectral resolving power ($\lambda/\Delta\lambda$) of ~1200, which converts to approximate full width at half max (FWHM) resolutions of ~0.5 cm^{-1} at 650 cm^{-1} and ~2.0 cm^{-1} at 2500 cm^{-1}. It scans from -49° to 49° across the track with 13.5-km ground footprints at the nadir view. This study uses AIRS level-1b calibrated radiances in the entire year of 2004.

For the purpose of validation, broadband OLR and sub-scene type information from the Aqua-CERES SSF Edition 3 are used. The strategy to collocate CERES and AIRS observations at

Atmos. Meas. Tech. Discuss., doi:10.5194/amt-2016-268, 2016
Manuscript under review for journal Atmos. Meas. Tech.
Published: 7 September 2016

the footprint level is the same as described in Huang et al. (2008). The CERES SSF algorithm employs a MODIS-imagery based algorithm to detect clear-sky footprint (Geier et al., 2003). The total precipitable water (TPW) in the CERES SSF data set is retrieved from the Special Sensor Microwave Imager (SSM/I; Goodberlet et al., 1990). Its lapse rate (ΔT) is derived from the GEOS Data Assimilation System (DAO, 1996). Surface skin temperatures (T_s) are estimated from MODIS clear-sky 11-μm radiance (Minnis et al., 2004). The CERES SSF algorithm uses ΔT, T_s, and TPW to define sub-scene types of clear-sky observations. Thus, the OLR can be inverted using appropriated broadband ADM and measured broadband radiances (Loeb et al., 2005; Kato and Loeb, 2005). Uncertainty of inverted CERES OLR is about 1% (Loeb et al., 2007).

The European Center for Medium range Weather Forecasting (ECMWF) ERA-Interim reanalysis (Dee et al., 2011) is used in this study as well. It has a spatial resolution of 1.5° latitude by 1.5° longitude and 37 vertical levels up to 1hPa. Similar to Huang et al. (2008) and Chen et al. (2013), the forward radiative transfer model used here is the MODerate resolution atmospheric TRANsmission code (MODTRAN, version 5; Anderson et al., 2007). MODTRAN is used to compute synthetic AIRS radiances and outgoing spectral fluxes at the top of atmosphere (TOA). MODTRAN 5 offers a spectral resolution as fine as 0.1 cm^{-1} (higher than AIRS spectral resolution). Compared with AIRS observations, MODTRAN 5 replicates AIRS brightness temperatures over 650-1600 cm^{-1} with mean difference of ~0.2 K (the AIRS noise equivalent delta temperature NEDT being 0.51 K over this band) (Anderson et al., 2007). AIRS radiances are generated by convoluting MODTRAN output and tabulated spectral response functions of AIRS channels (Strow et al., 2006). The TOA spectral fluxes are computed using a three-point Gaussian quadrature (Clough and Iacono, 1995).

Atmos. Meas. Tech. Discuss., doi:10.5194/amt-2016-268, 2016
Manuscript under review for journal Atmos. Meas. Tech.
Published: 7 September 2016

3. Algorithm for estimating clear-sky LW spectral flux: the case of nadir view

The algorithm for estimating clear-sky LW spectral flux from nadir-view AIRS spectral radiances consists of three steps. The first step is to use radiance alone to decide whether an AIRS spectrum can be considered as a clear-sky spectrum or not (usually referred as clear-sky detection). The second step is to classify the sub-scene type of a clear-sky spectrum using radiance information alone. The third step is to invert the AIRS radiances to spectral flux over the entire LW spectrum.

3.1. Clear-sky detection

3.1.1. Algorithm design

Detecting clear-sky scenes from IR radiance alone is usually done by applying a sequence of tests (Amato et al., 2014; and references therein). We use three tests in sequence for this purpose. Test 1 is a spatial inhomogeneous test commonly referred as the "Golden Arches" test proposed first by Coakley and Bretherton (1983). For a given AIRS footprint and four adjacent AIRS footprints, if the standard deviation of brightness temperatures at a window channel 963.8 cm^{-1} (hereafter denoted as $BT_{963.8}$) is smaller than a predetermined threshold value C1, the footprint passes Test 1. For the footprint that passes the "Golden Arches" test, Test 2 is a bi-spectral test, namely the brightness temperature difference between two narrow bands—one being 8 μm band (BT_8, 8.17-8.92 μm) and the other being 11 μm band (BT_{11}, 10.06-11.25 μm). Test 2 utilizes the spectrally dependent feature to distinguish cloudy spectrum and clear-sky spectrum, because the 11 μm band is sensitive to water clouds and ice clouds, while the 8 μm band has weak water vapor absorption lines, and the BT_8-BT_{11} difference has been widely used for this purpose (e.g. Ackerman and Strabala, 1994). If the BT_8-BT_{11} of an AIRS spectrum is less than a pre-determined value C2, the spectrum passes Test 2. Test 3 is a threshold test to compare the $BT_{963.8}$ with the surface temperature at the ground footprint interpolated from 6-hourly ERA-interim reanalysis, termed as Ts_{ERA}-$BT_{963.8}$. $BT_{963.8}$ is used as a surrogate of surface temperature in Chen and Huang (2014) because this channel has little atmospheric absorption in the case of clear sky. If Ts_{ERA}-$BT_{963.8}$ of an AIRS spectrum is smaller than a pre-determined value C3, the spectrum passes Test 3. Only when a spectrum passes all three tests, do we deem it to be a clear-sky spectrum. Note that, though ERA-interim reanalysis is used in this study, in future operational applications the reanalysis surface temperature can be replaced by the surface temperature from operational analysis.

We used four months of collocated AIRS and CERES nadir-view observations in 2006 to empirically determine the threshold values used in the three tests (i.e., C1, C2, and C3). In another words, we use the clear-sky footprint identified by CERES as the "ground truth" and decide the threshold values based on collocated AIRS observations accordingly. The four months used for this purpose are January, April, July, and October of 2006. A total of ~1.56 millions of collocated observations are available for this training purpose. We first categorize the observations into four groups: daytime ocean, nighttime ocean, daytime land, and nighttime land. Then for each group, the threshold value is defined as the value suitable for describing 95% of qualified observations. An example of how to decide C1 is given in Figure 1. Each panel plots the histogram of the standard deviation based on the $BT_{963.8}$ of the clear-sky AIRS footprint and four adjacent AIRS footprints. Only 5% of clear-sky observations in each panel have a standard deviation larger than the value denoted by the dash-dot line, which is then assigned as the value of C1. The value of C2 is decided in a similar manner. Water vapor continuum absorption is important for the AIRS channel at 963.8 cm^{-1}. Such absorption is dominated by humidity in the planetary boundary layer, which is highly correlated with surface temperature. Therefore, we divide observations further into different subgroups based on the value of Ts_{ERA} and the value of C3 is determined for each subgroup accordingly. Table 1 summarizes the threshold values for C1, C2, and C3 derived in this manner.

3.1.2. Performance of the clear-sky test algorithm

We assess the performance of the clear-sky test algorithm using collocated CERES and AIRS nadir-view observations in the entire year of 2004 (4.48 millions of observations in total). The performance is summarized in Table 2. The false negative (FN) rate refers to the percentage of collocated CERES clear-sky observations that have been classified as cloudy-sky observations by our algorithm. The false positive (FP) rate refers to the percentage of collocated CERES cloudy-sky observations that have been classified as clear-sky observations by our algorithm. The overall accuracy rate refers to the percentage of cases in which our algorithm can correctly classify the footprints. It can be seen that, although using three tests together increases the rate of false negative, such an approach is also effective in reducing the false positive rate. Given that the number of cloudy-sky observations is ~9-10 times more than that of clear-sky observations, using three tests together can achieve a better accuracy than using one of the tests alone. As far as the FN and FP rates are concerned, this algorithm is comparable to other clear-sky detection algorithms that are based on IR spectral radiances alone (e.g. Table 4 in Amato et al., 2014).

3.2. Sub-scene type classification

The second step in the overall algorithm is to classify the sub-scene types of clear-sky observations identified by the algorithm described in Section 3.1. The sub-scene types adopted here are largely similar to the discrete intervals defined by Table 3 in Loeb et al. (2005), which depend on the total precipitable water (TPW), surface temperature (T_s), and lapse rate (ΔT) defined as temperature difference between the surface and 300 hPa above it. Similar to Chen and Huang (2014), here $BT_{963.8}$ is used as a surrogate of surface temperature. ΔT is inferred from brightness temperature differences of two AIRS channels: 963.8 and 748.6 cm^{-1} (hereafter denoted as $\Delta BT_{963.8\text{ - }748.6}$). A quick estimate of TPW is obtained by a look-up-table approach proposed by Chen and Huang (2014), which makes use of double difference of two pairs of AIRS channels as well as $BT_{963.8}$ and $\Delta BT_{963.8\text{ - }748.6}$ to construct the look-up-table. Table 3 lists the accuracy of this algorithm based on the collocated AIRS and CERES observations in 2004 and the comparison with the auxiliary information of TPW, T_s, and ΔT in the CERES SSF dataset. It can be seen that, though this estimate method is solely based on AIRS radiances, the accuracy is 80% or even higher.

3.3. Estimate of fluxes from radiance measurements

The last component in our algorithm is to invert spectral fluxes from the AIRS radiances. Huang et al. (2008) adopted the same sub-scene type classification as in Loeb et al. (2005) for inverting AIRS radiance to spectral flux. Therefore, the algorithm in Huang et al. (2008) can be used here without further modification. Specifically, the spectral radiance ($I_{AIRS}(\theta)$ at each viewing zenith angle θ) is first converted to spectral flux (F_{AIRS}) over each AIRS channel using a pre-calculated spectral ADM ($R_{AIRS}(\theta)$) for each sub-scene type, $F_{AIRS} = \pi \cdot I_{AIRS}(\theta) / R_{AIRS}(\theta)$. Then a principle component-based multivariate prediction scheme is used to estimate spectral fluxes over the spectral portion not covered by the AIRS instrument. The performance of this radiance-to-flux algorithm and its characteristics has been documented in detail in Huang et al. (2008) and Chen et al. (2013).

4. Validation of the overall algorithm

This section focuses on validation of the overall algorithm in terms of its performance in estimating the spectral flux over the entire longwave spectrum. The following parts (1)-(3) examine the performance of the scene type classification algorithm, and part (4) examines the overall performance of the clear-sky detection and the scene type classification algorithms.

(1) We feed 6-hourly ERA-interim reanalysis data to the forward model to simulate clear-sky AIRS radiances and apply our algorithm to estimate the spectral flux (hereafter $F_{AIRS\text{-}only}$). We then compare this spectral flux with clear-sky spectral fluxes directly computed using the ECMWF ERA-Interim reanalysis with the same forward model (hereafter F_{ERA}). This is an idealized test because the forward modeling is assumed to be a surrogate of reality. Specifically, 6-hourly ERA-interim reanalysis data from January, April, July, and October 2004 are subsampled and interpolated onto the trajectory of AIRS nadir-view observations. Then MODTRAN5 is used to generate synthetic AIRS radiances and synthetic spectral flux F_{ERA}. Then $F_{AIRS\text{-}only}$ is derived from synthetic AIRS radiances based on the scene types determined from synthetic AIRS radiances alone, instead of directly determined from ERA profiles as in our previous works of Huang et al. (2008) and Chen et al. (2013). In total 290,761 profiles are used

Atmos. Meas. Tech. Discuss., doi:10.5194/amt-2016-268, 2016
Manuscript under review for journal Atmos. Meas. Tech.
Published: 7 September 2016

Atmospheric Measurement Techniques
Discussions

and the number of profiles for each sub-scene type varies from 50 to 64992. The averaged difference of the spectral flux for each scene type, denoted as $F_{AIRS\text{-}only}$ - F_{ERA}, at 10 cm^{-1} spectral interval is shown in Figure 2. For the window bands, the differences ($F_{AIRS\text{-}only}$ - F_{ERA}) are generally within ± 0.03 Wm^{-2} per 10 cm^{-1}. Exceptions are seen for those sub-scene types with very dry atmosphere above a hot surface. These circumstances make it difficult for our radiance-based algorithm to faithfully estimate the TPW. As shown in Table 3, the frequency of occurrences for such scene types is small, e.g., hot surface with temperature above 310 K is no more than 2%. Outside the window bands, the $F_{AIRS\text{-}only}$ - F_{ERA} differences are usually within ±0.02 Wm^{-2} per 10 cm^{-1}.

(2) For collocated AIRS and CERES clear-sky observations in 2004, we use the algorithm to derive the spectral flux and OLR (the summation of spectral flux) from AIRS radiance (hereafter, $OLR_{AIRS\text{-}only}$) and compare it with the collocated CERES clear-sky OLR (hereafter OLR_{CERES}). Upper panels in Figure 3 show the annual-mean daytime and nighttime difference between $OLR_{AIRS\text{-}only}$ and OLR_{CERES}, respectively. The differences are averaged onto 2° latitude by 2.5° longitude grids from 80°S to 80°N. Lower panels in Figure 3 show the histograms of $OLR_{AIRS\text{-}only}$-OLR_{CERES} differences for all collocated AIRS and CERES clear-sky footprints. Figure 3a and 3b show that the difference tends to be negative over land areas (~1-2 Wm^{-2}) and positive over extra-tropical oceans (~1-3 Wm^{-2}). The RMS (root-mean-square) differences for Figure 3a and 3b are 1.79 and 1.11 Wm^{-2}, respectively. Such pattern and magnitude of the differences in Figure 3a and 3b are comparable to the results using the scene type information directly from the CERES SSF data set, as shown in Figure 5a and 5b in Chen et al. (2013). In terms of the statistics of $OLR_{AIRS\text{-}only}$ – OLR_{CERES} difference for individual footprint, the daytime mean

difference is 0.91 Wm^{-2} with a standard deviation of 2.34 Wm^{-2} (Figure 3c) and the nighttime mean difference is 0.14 Wm^{-2} with a standard deviation of 1.85 Wm^{-2} (Figure 3d). These statistics are comparable to those in Huang et al. (2008) and Chen et al. (2013).

(3) We examine the statistics of $OLR_{AIRS\text{-}only}$ - OLR_{CERES} differences for each available clear-sky sub-scene type in the data used in part (2). The results are summarized in Figure 4. The averaged daytime $OLR_{AIRS\text{-}only}$ - OLR_{CERES} differences for all sub-scene types are between -1.6 Wm^{-2} and 3.3 Wm^{-2} with a standard deviation no larger than 3.8 Wm^{-2}. For the nighttime, the mean difference for all sub-scene types varies from -0.7 Wm^{-2} to 2.2 Wm^{-2} and the standard deviation is less than 2.5 Wm^{-2}. Given that the radiometric uncertainty of CERES OLR is about 1% and typical OLR value varies between 200-300 Wm^{-2}, the mean differences (black line in Figure 4) are within or at least comparable to the radiometric uncertainty of CERES OLR (red line in Figure 4).

(4) In addition to using collocated clear-sky observations to evaluate the algorithm, we also apply the algorithm to all collocated AIRS and CERES nadir-view observations in the entire year of 2004 and obtain OLR for all AIRS measurements that our algorithm determines to be clear-sky observations. The mean difference is 1.52 Wm^{-2} and standard deviation is 2.46 Wm^{-2}. The figure is not shown here. We then compare the OLR of those "false positive" observations, i.e. footprints identified as clear-sky scenes by our algorithm but as cloudy-sky scenes by the CERES algorithm. Figure 5 shows the histograms of OLR differences ($OLR_{AIRS\text{-}only}$ – OLR_{CERES}) of such cases of "false positive". The mean difference is 2.93 Wm^{-2} and 1.60 Wm^{-2} for the daytime and nighttime, respectively. The standard deviation is 2.3 Wm^{-2} for both cases. The mean OLR for the cases shown in Figure 5a and 5b is 288.7 Wm^{-2} and 279.0 Wm^{-2}, respectively, which

Atmos. Meas. Tech. Discuss., doi:10.5194/amt-2016-268, 2016
Manuscript under review for journal Atmos. Meas. Tech.
Published: 7 September 2016

means the relative difference between $OLR_{AIRS\text{-}only}$ and OLR_{CERES} is only 1.0% and 0.6%. This suggests that, even though the algorithm misclassifies such cloudy-sky observations as clear-sky ones, the estimated OLR difference between $OLR_{AIRS\text{-}only}$ and OLR_{CERES} is only 1% or less.

5. Applicability to other viewing zenith angles (VZAs)

The algorithm described above is for nadir-view AIRS radiances. It can be extended to other viewing zenith angles by taking the dependency of upwelling radiances on viewing zenith angles into account. Specifically, for the first two steps depicted in Section 3, the threshold values and look-up-tables need to be adjusted in accordance with the viewing zenith angles. The algorithm in the third component has already taken viewing zenith angle into account (Huang et al., 2008) and thus no additional effort is needed. Since the objective of this study is to demonstrate the feasibility of the algorithm, we summarize the performance of the algorithm for other VZAs instead of describing all details as done for the case of nadir-view observations. Figure 6a shows the success rate for the algorithm to accurately classify cloudy and clear-sky footprints as a function of the VZA, which still uses the collocated CERES scene type information as ground truth. The algorithm performs consistently across all VZAs; when the VZA increases from zero to 45^{o}, the success rate varies within 2%. Figure 6b shows the differences between $OLR_{AIRS\text{-}only}$ and OLR_{CERES} for both daytime and nighttime results. Both differences, 1.93-2.15 Wm^{-2} for daytime and 1.07-1.67 Wm^{-2} for nighttime, change little with respect to the VZA.

The performance with respect to different VZAs here is consistent with previous results in Huang et al. (2008) and Chen et al. (2013), two studies that rely on the sub-scene type

Atmos. Meas. Tech. Discuss., doi:10.5194/amt-2016-268, 2016
Manuscript under review for journal Atmos. Meas. Tech.
Published: 7 September 2016

information from the CERES SSF dataset. The algorithm in this study behaves robustly across the range of VZAs for AIRS measurements. The other hyperspectral sounders make observations over the similar range of VZAs. Therefore, the robust performances here further assure the potential of extending the algorithm to other hyperspectral sounding observations.

6. Conclusions and discussion

Using AIRS observation as an example, this study develops an algorithm based solely on spectral radiances to estimate LW clear-sky spectral flux. The algorithm first detects clear-sky spectrum by a three-step threshold test, i.e., the "Golden Arches" test for the spatial homogeneity, a bi-spectral test for spectral features of clear-sky absorption and emission, and a single-channel thermal threshold test for an extra check against surface temperature. Atmospheric and surface parameters (total precipitable water, lapse rate and surface temperature) needed for categorizing sub-scene types are directly estimated using AIRS radiances at six channels and the pre-constructed lookup tables. The accuracy of clear-sky detection and sub-scene type classification, and their effect on clear-sky spectral flux derivation have been assessed. When using CERES scene type information as the ground truth, the algorithm can achieve an accuracy rate of 88.7% for classifying nadir-view clear-sky and cloudy footprints. Differences between OLR derived using the algorithm and the collocated CERES OLR show no strong dependence on the sub-scene types. The statistics of $OLR_{AIRS\text{-}only}$ - OLR_{CERES} obtained here are comparable to those in Huang et al. (2008) and Chen et al. (2013), two studies that directly used the scene-type and clear-sky information from the CERES data set. The algorithm performs consistently over different viewing zenith angles.

Atmos. Meas. Tech. Discuss., doi:10.5194/amt-2016-268, 2016
Manuscript under review for journal Atmos. Meas. Tech.
Published: 7 September 2016

The purpose of this study is to explore the additional value of hyperspectral sounding measurements, i.e., by deriving spectral flux directly from such observations as the spectral fluxes that have been shown to have unique merit in climate model evaluations (Huang et al., 2006; Huang et al., 2013; Huang et al., 2014). The broadband flux measured by CERES and its predecessor ERBE has become a benchmark standard in the earth observation community, so does the sophisticated and well-validated multiple data-fusion approach used in the CERES data product. It is not the intention of this study to produce merely another set of broadband flux products. Instead, the emphasis here is to derive the spectral flux, which can help us understand the compensating biases in modeled broadband radiation flux.

In general, the performance of the algorithm is more affected by the accuracy of clear-sky detection than the rest of components. To use LW spectral observations alone to detect clear sky is not easy, partially because it is difficult to distinguish optically thin clouds or small fraction of clouds within the field of view. In operational use, the accuracy of clear-sky detection could be improved if other simultaneous measurements, especially those made at higher spatial resolutions, are available. A good example is the use of MODIS imageries in the CERES SSF algorithm. Another example is the use of microwave sounding observations to help the surface parameter retrievals, which in turn helps the retrievals of atmospheric parameters including the cloud vs. clear-sky detection (Kahn et al., 2014).

While the algorithm presented in this study is only for clear-sky spectra, it is conceivable that this algorithm can be evolved for estimating spectral fluxes from cloudy-sky hyperspectral observations as well. In the case of cloudy-sky spectra, the cloud parameters, especially cloud fraction and cloud top height, will need to be considered in the definition of sub-scene types.

Atmos. Meas. Tech. Discuss., doi:10.5194/amt-2016-268, 2016
Manuscript under review for journal Atmos. Meas. Tech.
Published: 7 September 2016

The rich information contained in hyperspectral radiances is likely sufficient to define sub-scene types needed for the algorithm.

Acknowledgments

The AIRS Level 1B data are downloaded from NASA GSFC DAAC and the Aqua CERES data were obtained from NASA Langley DAAC. The ECMWF ERA-interim data are from http://data-portal.ecmef.int/data/d/. This research is supported by NASA under Grants NNX14AJ50G and NNX15AC25G awarded to the University of Michigan.

Atmos. Meas. Tech. Discuss., doi:10.5194/amt-2016-268, 2016
Manuscript under review for journal Atmos. Meas. Tech.
Published: 7 September 2016

Atmospheric Measurement Techniques Discussions

References:

Ackerman, S. A., and Strabala, K. I.: Satellite remote sensing of H_2SO_4 aerosol using the 8- to 12-µm window region: Application to Mount Pinatubo. J Geophys Res Atmos, 99, 18639–18649, 1994.

Amato, U., Lavanant, L., Liuzzi, G., Masiello, G., Serio, C., Stuhlmann, R. and Tjemkes, S. A.: Cloud mask via cumulative discriminant analysis applied to satellite infrared observations: scientific basis and initial evaluation. Atmos Meas Tech, 7, 3355–3372, 2014.

Anderson, G. P., Berk, A., Chetwynd, J. H., Harder, J., Fontenla, J. M., Shettle, E. P., Saunders, R., Snell, H. E., Pilewskie, P., Kindel, B. C., Gardner, J. A., Hoke, M . L., Felde, G. W., Lockwood, R. B., Acharya, P. K.: Using the MODTRAN5 radiative transfer algorithm with NASA satellite data: AIRS and SORCE. Algorithms and Technologies for Multispectral, Hyperspectral, and Ultraspectral Imagery XIII. SPIE, 6565, doi:10.1117/ 12.721184, 2007.

Aumann, H. H., Chahine, M. T., Gautier, C., Goldberg, M. Dl, Kalnay, E., McMillin, L. M., Revercomb, H., Rosenkranz, P. W., Smith, W. L., Staelin, D. H., Strow, L. L., and Susskind, J.: AIRS/AMSU/HSB on the aqua mission: Design, science objectives, data products, and processing system. IEEE Trans Geosci Remote Sens, 41,253–264, 2003.

Barkstrom, B. R.: The Earth Radiation Budget Experiment (ERBE). Bull Amer Meteor Soc, 65, 1170–1185, 1984.

Atmos. Meas. Tech. Discuss., doi:10.5194/amt-2016-268, 2016
Manuscript under review for journal Atmos. Meas. Tech.
Published: 7 September 2016

Atmospheric Measurement Techniques
Open Access
EGU
Discussions

Chen, X. H. and Huang, X. L.: Usage of differential absorption method in the thermal IR: a case study of quick estimate of clear-sky column water vapor. J Quant Spectrosc Radiat Transfer, 104, 99-106, 2014.

Chen, X. H., Huang, X. L., Loeb, N. G., Wei, H. L.: Comparisons of clear-sky outgoing far-IR flux inferred from satellite observations and computed from three most recent reanalysis products. J Climate, 26(2), 478-494, doi:10.1175/JCLI-D-12-00212.1, 2013.

Clough, S. A., and Iacono, M. J.: Line-by-line calculations of atmospheric fluxes and cooling rates II: Application to carbon dioxide, ozone, methane, nitrous oxide, and the halocarbons. J Geophys Res Atmos, 100 (D8), 16519–16535, 1995.

Coakley, J. A. and Bretherton, F. P.: Cloud cover from high-resolution scanner data: Detecting and allowing for partially filled fields of view. J Geophys. Res., 87, 4917-4932, 1983.

DAO: Algorithm Theoretical Basis Document for Goddard Earth Observing System Data Assimilation System (GOES DAS) With a Focus Version 2. Data Assimilation Off., NASA Goddard Space Flight Cent, Greenbelt, Md., p. 310, 1996.

Dee, D. P., Uppala, S. M., Simmons, A. J., Berrisford, P., Poli, P., Kobayashi, S., Andrae, U., Balmaseda, M. A., Balsamo, G., Bauer, P., Bechtold, P., Beljaars, A. C. M., van de Berg, L., Bidlot, J., Bormann, N., Delsol, C., Dragani, R., Fuentes, M., Geer, A. J., Haimberger, L., Healy, S. B., Hersbach, H., Hólm, E. V., Isaksen, L., Kållberg, P., Köhler, M., Matricardi, M., McNally, A. P., Monge-Sanz, B. M., Morcrette, J.-J., Park, B.-K., Peubey, C., de Rosnay, P., Tavolato, C., Thépaut, J.-N., Vitart, F.: The ERA-Interim reanalysis configuration and performance of the data assimilation system. Q J R Meteorol Soc, 137, 553–597, 2011.

Dessler, A. E., Yang, P., Lee, J., Solbrig, J., Zhang, Z., and Minschwaner, K: An analysis of the dependence of clear-sky top-of-atmosphere outgoing longwave radiation on atmospheric temperature and water vapor. J Geophys Res Atmos, 113, D17102, doi:10.1029/2008JD010137, 2008.

Geier, E. B., Green, R. N., Miler, W. F., Nolan, S. K., and Franklin, C. B.: CERES Data Management System: Single Satellite Footprint TOA/Surface Fluxes and Clouds (SSF) Collection Documents Release 2, Version 6. Radiat and Aerosols Branch, Atmos Sci, NASA Langley Res. Cent., Hampton, Va., p.194, 2003.

Goodberlet, M. A., IEEE, Member, Swift, C. T., IEEE, Fellow, and Wilkerson, J. C.: Ocean surface wind-speed measurements of the Special Sensor Microwave Imager (SSM/I). IEEE Trans Geosci Remote Sens, 28, 823–828, doi:10.1109/36.58969, 1990.

Han, Y., Revercomb, H., Cromp, M., Gu, D. G., Johnson, D., Mooney, D., Scott, D., Strow, L., Bingham, G., Borg, L., Chen, Y., DeSlover, D., Esplin, M., Hagan, D., Jin, X., Knuteson, R., Motteler, H., Predina, J., Suwinski, L., Taylor, J., Tobin, D., Tremblay, D., Wang, C. M., Wang, L. H., Wang, L. K., Zavyalov, V.: Suomi NPP CrIS measurements, sensor data record algorithm, calibration and validation activities, and record data quality. J Geophys Res Atmos, doi:10.1002/2013JD020344, 2013.

Hilton, F., Armante, R., August, T., Barnet, C., Bouchard, A., Camy-Peyret, C., Capelle, V., Clarisse, L., Clerbaux, C., Coheur, P.-F.,Collard, A., Crevoisier, C., Goldberg, M., Guidard, V., Hurtmans, D., Illingworth, S., Jacquinet-Husson, N., Kerzenmacher, T., Klaes, D., Lavanant, L., Masiello, G., Matricardi, M., Mcnally, A., Newman, S., Pavelin, E., Payan, S., Péquignot, E., Peyridieu,

Atmos. Meas. Tech. Discuss., doi:10.5194/amt-2016-268, 2016
Manuscript under review for journal Atmos. Meas. Tech.
Published: 7 September 2016

S., Phulpin, T., Remedios, J., Schlüssel, P., Serio, C., Strow, L., Stubenrauc, C., Taylor, J., Tobin, D., Wolf, W., and Zhou, D.: Hyperspectral Earth Observation from IASI: Five Years of Accomplishments. Bull Amer Meteor Soc, 93, 347–370, doi: 10.1175/BAMS-D-11-00027.1, 2012.

Huang, X. L., Chen, X. H., Potter, G. L., Oreopoulos, L., Cole, J. N. S., Lee, D. M., Loeb, N. G.: A global climatology of outgoing longwave spectral cloud radiative effect and associated effective cloud properties. J Climate, 27, 7475-7492. doi: 0.1175/JCLI-D-13-00663.1, 2014.

Huang, X. L., Cole, J. N.S., He, F., Potter, G. L., Oreopoulos, L., Lee, D.M., Suarez, M., Loeb, N.G.: Longwave band-by-band cloud radiative effect and its application in GCM evaluation. J Climate, 26(2), 450-467, doi:10.1175/JCLI-D-12-00112.1, 2013.

Huang, X. L., Loeb, N. G., and Yang, W. Z: Spectrally resolved fluxes derived from collocated AIRS and CERES measurements and their application in model evaluation, Part II: cloudy sky and band-by-band cloud radiative forcing over the tropical oceans. J Geophys Res Atmos, 115. doi:10.1029/2010JD013932, 2010.

Huang, X. L ., Ramaswamy, V. and Schwarzkopf, M. D.: Quantification of the source of errors in AM2 simulated tropical clear-sky outgoing longwave radiation. J Geophys Res Atmos, 111, D14107, doi:10.1029/2005JD006576, 2006.

Huang, X. L., Yang, W. Z., Loeb, N. G., and Ramasawamy, V.: Spectrally resolved fluxes derived from collocated AIRS and CERES measurements and their application in model evaluation: clear sky over the tropical oceans. J Geophys Res Atmos, 113, D09110, doi:10.1029/ 2007JD009219, 2008.

Atmos. Meas. Tech. Discuss., doi:10.5194/amt-2016-268, 2016
Manuscript under review for journal Atmos. Meas. Tech.
Published: 7 September 2016

Kahn, B. H, Irion, F. W., Dang, V.T., Manning, E. M., Nasiri, S. L., Naud, C. M., Blaisdell, J. M., Schreier, M. M., Yue, Q., Bowman, K. W., Fetzer, E. J., Hulley, G. C., Liou, K. N., Lubin, D., Ou, S. C., Susskind, J., Takano, Y., Tian, B. and Worde, J. R.: The atmospheric infrared sounder version 6 cloud products. Atmos Chem Phys, 14, 399 –426, 2014.

Kato, S. and Loeb, N. G.: Top-of-atmosphere shortwave broadband observed radiance and estimated irradiance over polar regions from Clouds and the Earth's Radiant Energy System (CERES) instruments on Terra. J Geophys Res Atmos,110, D07202, doi:10.1029/2004JD005308, 2005.

Loeb, N. G., Kato, S., Loukachine, K., Manalo-Smith, N., and Doelling. D. R: Angular distribution models for top-of-atmosphere radiative flux estimation from the Clouds and the Earth's Radiant Energy System instrument on the Terra satellite. Part I: Methodology. J Atmos Oceanic Technol, 22, 338–351, 2005.

Loeb, N. G., Kato, S., Loukachine, K., Manalo-Smith, N., and Doelling, D. R.: Angular distribution models for top-of-atmosphere radiative flux estimation from the Clouds and the Earth's Radiant Energy System instrument on the Terra satellite. Part II: Validation. J Atmos Oceanic Tech, 24, 564-584, 2007.Minnis, P., Young, D. F., Sun-Mack, S., Heck, P. W., Doelling, D. R., and Trepte, Q.: CERES Cloud Property Retrievals from Imagers on TRMM, Terra, and Aqua. SPIE, 5235, 37–48, 2004.

Moy, L. A., Knuteson, R. O., Tobin, D. C., Revercomb, H. E., Borg, L. A., and Susskind, J.: Comparison of measured and modeled outgoing longwave radiation for clear-sky ocean

Atmos. Meas. Tech. Discuss., doi:10.5194/amt-2016-268, 2016
Manuscript under review for journal Atmos. Meas. Tech.
Published: 7 September 2016

and land scenes using coincident CERES and AIRS observations. J Geophys Res Atmos, 115, D15110, doi:10.1029/2009JD012758, 2010.

O'Carroll, A. G., August, T., Borgne, P. L., and Marsouin, A.: The accuracy of SST retrievals from Metop-A IASI and AVHRR using the EUMETSAT OSI-SAF matchup dataset, Remote Sensing of Environment , 126, 184–194, doi:10.1016/j.rse.2012.08.006, 2012.

Susskind, J., Molnar, G., Iredell, L., and Loeb, N. G.: Interannual variability of outgoing longwave radiation as observed by AIRS and CERES. J Geophys Res Atmos, 117, D23107, doi:10.1029/2012JD017997, 2012.

Strow, L. L., Hannon, S. E., De-Souza Machado S., Motteler, H. E., and Tobin, D. C.: Validation of the Atmospheric Infrared Sounder radiative transfer algorithm. J Geophys Res Atmos, 111, D09S06, doi:10.1029/2005JD006146, 2006.

Strow, L. L., Motteler, H., Tobin, D., Revercomb, H., Hannon, S., Buijs, H., Predina, J., Suwinski, L., and Glumb, R.: Spectral calibration and validation of the Cross-track Infrared Sounder (CrIS) on the Suomi NPP satellite. J Geophys Res Atmos, 118:12486–12496, doi:10.1002/2013JD020480, 2013.

Wang, L. K., Trenblay, D. A., Han, Y., Esplin, M., Hagan, D. E., Predina, J., Suwinski, L., Jin, X., and Chen, Y.: Geolocation assessment for CrIS sensor data records. J. Geophys. Res. Atmos., 118, 12690-12704, doi:10.1002/2013jd020376, 2013.

Atmos. Meas. Tech. Discuss., doi:10.5194/amt-2016-268, 2016
Manuscript under review for journal Atmos. Meas. Tech.
Published: 7 September 2016

Atmospheric Measurement Techniques Discussions

Wielicki, B. A., Barkstrom, B. R., Harrison, E. F., Smith, G. L., and Cooper, J. E.: Clouds and the Earth's radiant energy system (CERES): An Earth observing system experiment. Bull Amer Meteor Soc,77, 853–868, 1996.

Atmos. Meas. Tech. Discuss., doi:10.5194/amt-2016-268, 2016
Manuscript under review for journal Atmos. Meas. Tech.
Published: 7 September 2016

Atmospheric Measurement Techniques Discussions

Table 1. Threshold values used in the clear-sky tests. Details of threshold definitions and the ways to determine them can be found in Section 3.1.

Thresholds	**Daytime Ocean**	**Nighttime Ocean**	**Daytime Land**	**Nighttime Land**
C1 (K)	0.62	0.61	2.17	1.650
C2 (K)	-1.39	-1.38	-2.04	-0.510
C3 (K)	2.47 (Ts_{ERA}<280 K) 3.12 (280-285 K) 3.61 (285-290 K) 3.61 (290-295 K) 3.95 (295-300 K) 5.49 (> 300 K)	2.29(Ts_{ERA}<280 K) 3.12 (280-285 K) 3.11 (285-290 K) 3.54 (290-295 K) 4.13 (295-300 K) 5.82(>300 K)	1.24 (Ts_{ERA}<290 K) 1.49 (290-295 K) 3.28 (295-300 K) 3.99 (300-305 K) 5.31 (305 -310 K) 5.76 (>310 K)	2.28 (Ts_{ERA}<260 K) 5.41 (260-270 K) 5.61 (270-275 K) 6.72 (275 -280 K) 7.36(280-285 K) 8.25 (>285 K)

Table 2. The performance of clear-sky detection algorithm. FN (false negative) is the percentage of CERES clear-sky observations misclassified as cloudy sky by the algorithm. FP (false positive) is the percentage of CERES cloudy-sky observations misclassified as clear sky by the algorithm. Accuracy is the overall success rate compared to the CERES algorithm in terms of distinguishing clear- vs. cloudy-sky observations. Steps 1-3 are defined in detail in Section 3.1.

	Ocean			**Land**			**Near-globe (81°S-81°N)**		
	FN (%)	FP (%)	Accuracy (%)	FN (%)	FP (%)	Accuracy (%)	FN (%)	FP (%)	Accuracy (%)
Step 1	4.8	19.7	81.3	6.2	33.1	71.1	5.4	22.4	79.1
Steps 1+2	9.7	14.1	86.2	10.0	19.2	82.2	9.8	15.2	85.3
Steps 1+2+3	13.9	10.0	89.8	14.0	15.4	84.8	13.9	11.1	88.7

Atmos. Meas. Tech. Discuss., doi:10.5194/amt-2016-268, 2016
Manuscript under review for journal Atmos. Meas. Tech.
Published: 7 September 2016

Atmospheric Measurement Techniques Discussions

Table 3. Accuracy of the sub-scene type classification algorithm described in subsection 3.2. The statistics are based on collocated nadir-view AIRS and CERES observations in 2004. 'Occ.' and 'Acc.' in the Table denotes occurrence and accuracy, respectively. The sub-scene type is coded as a three-digit number. The first digit refers to TPW, the second one refers to ΔT, and the last refers to T_s, as defined in the table. The definition of sub-scene types here is identical to the LW discrete intervals in Loeb et al. (2005).

Sub-scene type	**TPW (cm)**	**Occ. (%)**	**Acc. (%)**	**Sub-scene type**	**ΔT (K)**	**Occ. (%)**	**Acc. (%)**	**Sub-scene type**	**T_s (K)**	**Occ. (%)**	**Acc. (%)**
1--	0-1	16.3	63.1	**-1-**	<15	32.9	70.5	**--1**	<270	1.24	99.8
2--	1-3	55.0	86.8	**-2-**	15-30	65.8	85.1	**--2**	270-290	24.7	98.2
3--	3-5	25.7	82.0	**-3-**	30-45	1.29	48.4	**--3**	290-310	73.1	93.2
4--	>5	3.0	53.8	**-4-**	>45	0.002	16.7	**--4**	310-330	0.98	22.1
								--5	>330	0.0	-
Overall		100	80.7			100	79.8			100	93.8

Atmos. Meas. Tech. Discuss., doi:10.5194/amt-2016-268, 2016
Manuscript under review for journal Atmos. Meas. Tech.
Published: 7 September 2016

Atmospheric Measurement Techniques Discussions

Figure Captions

Figure 1. Histogram of the standard deviations of 963.8 cm^{-1} brightness temperatures among an AIRS clear-sky footprint and four adjacent AIRS footprints derived. The clear-sky information from collocated CERES observation is used. The histograms for daytime ocean, daytime land, nighttime ocean, and nighttime land are plotted separately. The black dash line denotes the 95% percentile and corresponds to the value of C1 shown in Table 1.

Figure 2. The mean differences between the predicted spectral fluxes based on synthetic AIRS spectra and the directly computed fluxes for different sub-scene types. The naming convention of sub-scene type is defined in Table 3. The spectral flux is for every 10 cm^{-1} interval from 10 cm^{-1} to 2000 cm^{-1}.

Figure 3. (a) Near-global distribution of annual-mean differences between daytime OLR derived from clear-sky AIRS nadir-view radiances using the algorithm in this study and the collocated CERES clear-sky daytime OLR ($OLR_{AIRS\text{-}only}$ - OLR_{CERES}). The data in 2004 is used and averaged onto 2.5° longitude by 2° latitude grids. (b) Same as (a) but for annual-mean nighttime OLR differences. (c) The histograms of daytime $OLR_{AIRS\text{-}only}$ - OLR_{CERES} differences among all collocated AIRS and CERES nadir-view footprints. (d) Same as (c) but for the histogram of nighttime $OLR_{AIRS\text{-}only}$ - OLR_{CERES} differences. Fifty bins are used in both (c) and (d). The mean differences ± standard deviations and number of observations are also labeled on the plot.

Figure 4. (a) Black line denotes the mean of daytime OLR difference ($OLR_{AIRS\text{-}only}$ - OLR_{CERES}) for each sub-scene type. Ticked vertical lines denote ±1σ (standard deviation). Red line is the uncertainty of OLR_{CERES} (assuming 1% of mean OLR_{CERES} for all scene types). Blue bars indicate the frequency of occurrence of each sub-scene type in percentage. (b) Same as (a) but for

nighttime observations. The numbers of daytime and nighttime observations are 1.86×10^5 and 1.87×10^5, respectively.

Figure 5. (a) and (b) are similar as Figure 3(c) and 3 (d) but for the AIRS footprints classified as clear sky by the algorithm in this study while their collocated CERES footprints are identified as cloudy sky. Mean ± standard deviation of the difference ($OLR_{AIRS\text{-}only} – OLR_{CERES}$) is also given on the plot.

Figure 6. (a) Success rate of the algorithm in distinguishing clear-sky and cloudy-sky footprints as a function of viewing zenith angle (VZA). (b) The difference of $OLR_{AIRS\text{-}only} – OLR_{CERES}$ as a function of VZA. Ticked vertical lines denote the $\pm1\sigma$ (standard deviation).

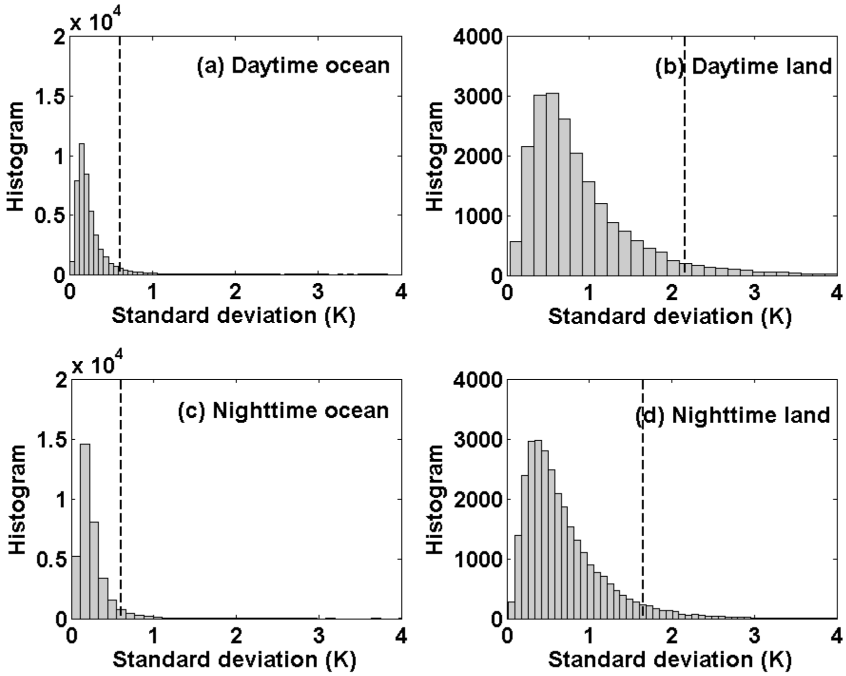

Figure 1. Histogram of the standard deviations of 963.8 cm^{-1} brightness temperatures among an AIRS clear-sky footprint and four adjacent AIRS footprints derived. The clear-sky information from collocated CERES observation is used. The histograms for daytime ocean, daytime land, nighttime ocean, and nighttime land are plotted separately. The black dash line denotes the 95% percentile and corresponds to the value of C1 shown in Table 1.

Atmos. Meas. Tech. Discuss., doi:10.5194/amt-2016-268, 2016
Manuscript under review for journal Atmos. Meas. Tech.
Published: 7 September 2016

Atmospheric Measurement Techniques
Discussions
Open Access

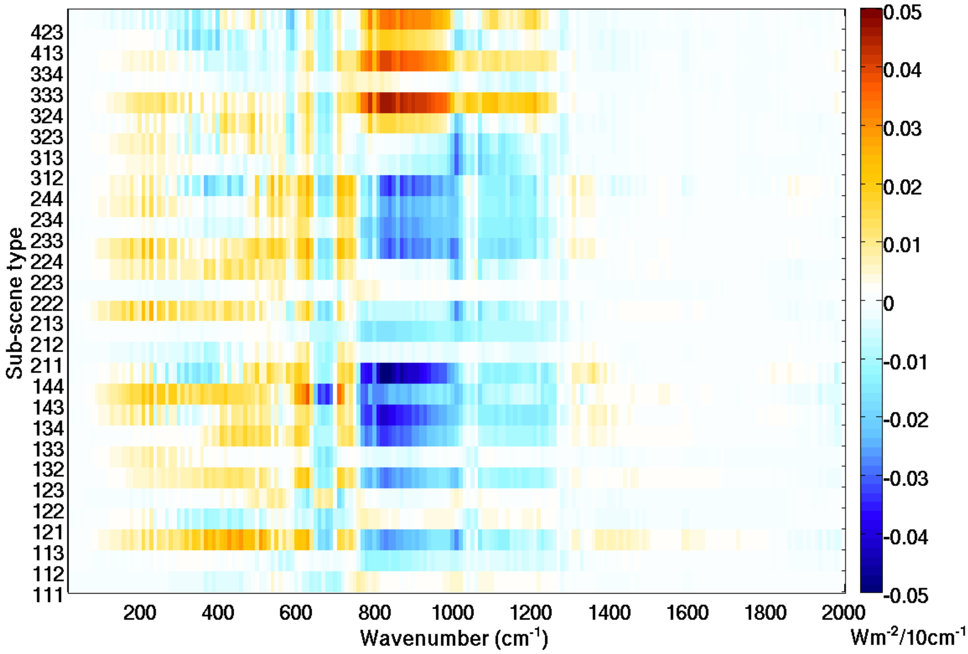

Figure 2. The mean differences between the predicted spectral fluxes based on synthetic AIRS spectra and the directly computed fluxes for different sub-scene types. The naming convention of sub-scene type is defined in Table 3. The spectral flux is for every 10 cm^{-1} interval from 10 cm^{-1} to 2000 cm^{-1}.

Atmos. Meas. Tech. Discuss., doi:10.5194/amt-2016-268, 2016
Manuscript under review for journal Atmos. Meas. Tech.
Published: 7 September 2016

Atmospheric Measurement Techniques
Discussions

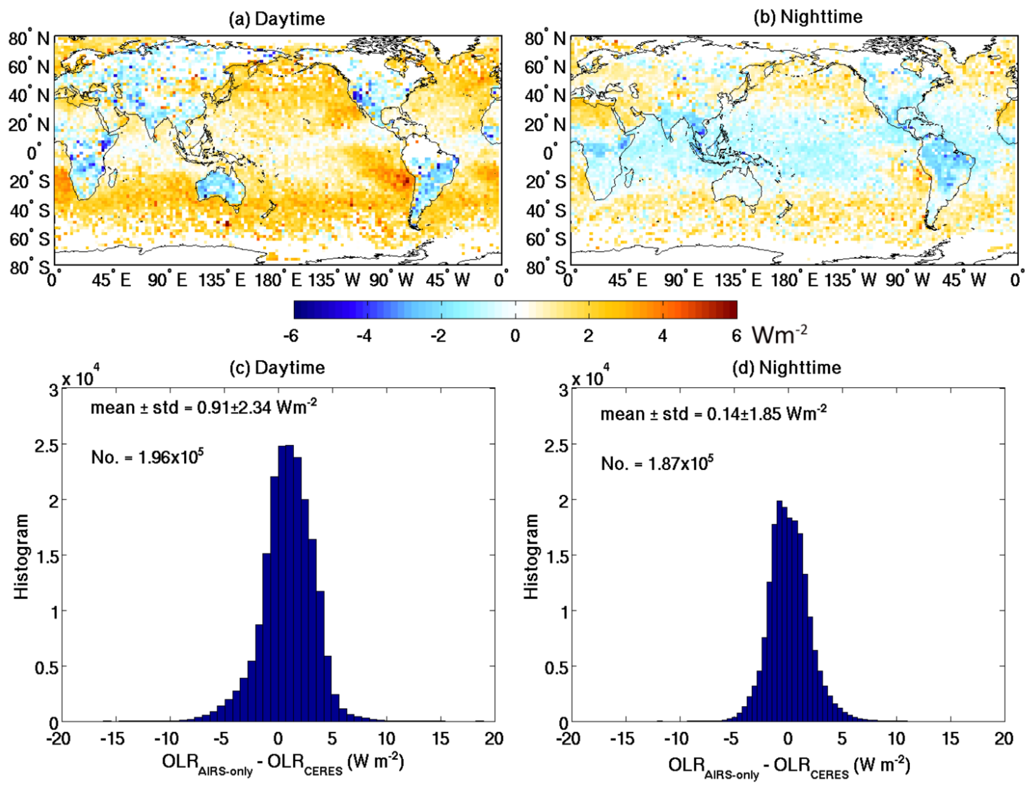

Figure 3. (a) Near-global distribution of annual-mean differences between daytime OLR derived from clear-sky AIRS nadir-view radiances using the algorithm in this study and the collocated CERES clear-sky daytime OLR (OLR$_{AIRS\text{-}only}$ - OLR$_{CERES}$). The data in 2004 is used and averaged onto 2.5° longitude by 2° latitude grids. (b) Same as (a) but for annual-mean nighttime OLR differences. (c) The histograms of daytime OLR$_{AIRS\text{-}only}$ - OLR$_{CERES}$ differences among all collocated AIRS and CERES nadir-view footprints. (d) Same as (c) but for the histogram of nighttime OLR$_{AIRS\text{-}only}$ - OLR$_{CERES}$ differences. Fifty bins are used in both (c) and (d). The mean differences ± standard deviations and number of observations are also labeled on the plot.

Atmos. Meas. Tech. Discuss., doi:10.5194/amt-2016-268, 2016
Manuscript under review for journal Atmos. Meas. Tech.
Published: 7 September 2016

Atmospheric Measurement Techniques Discussions
Open Access

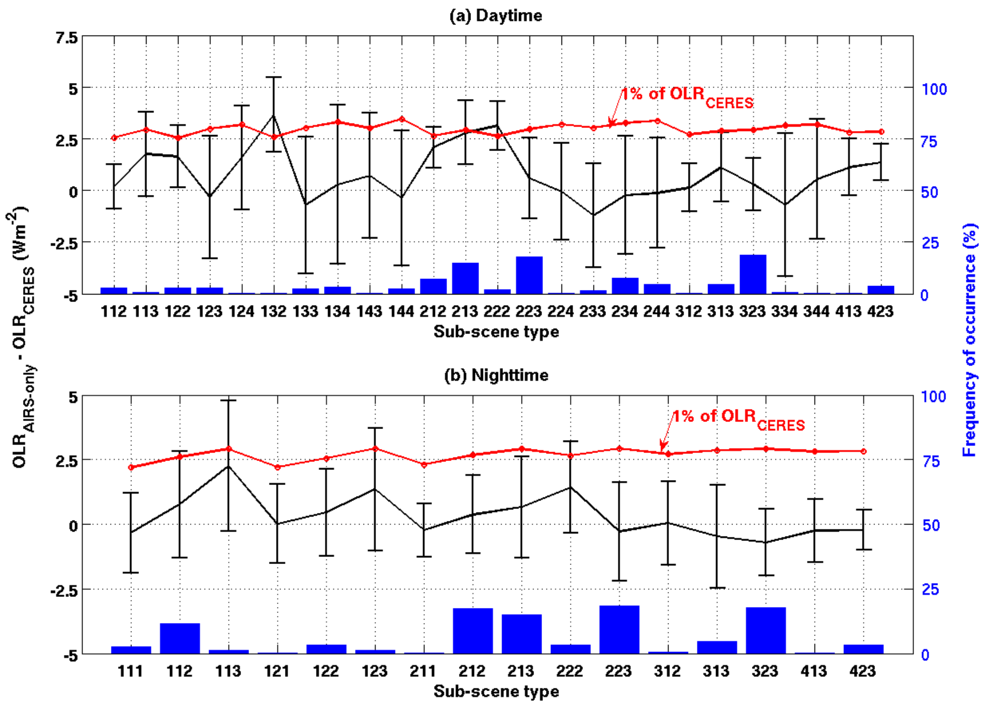

Figure 4. (a) Black line denotes the mean of daytime OLR difference ($OLR_{AIRS\text{-}only}$ - OLR_{CERES}) for each sub-scene type. Ticked vertical lines denote ±1σ (standard deviation). Red line is the uncertainty of OLR_{CERES} (assuming 1% of mean OLR_{CERES} for all scene types). Blue bars indicate the frequency of occurrence of each sub-scene type in percentage. (b) Same as (a) but for nighttime observations. The numbers of daytime and nighttime observations are 1.86×10^5 and 1.87×10^5, respectively.

Atmos. Meas. Tech. Discuss., doi:10.5194/amt-2016-268, 2016
Manuscript under review for journal Atmos. Meas. Tech.
Published: 7 September 2016

Atmospheric Measurement Techniques
Discussions

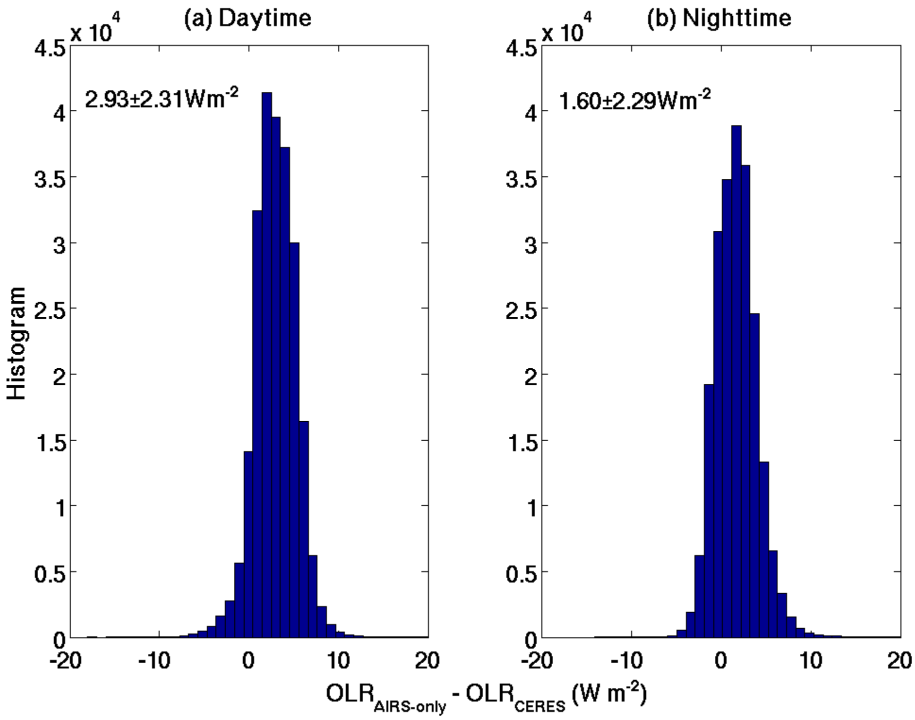

Figure 5. (a) and (b) are similar as Figure 3(c) and 3 (d) but for the AIRS footprints classified as clear sky by the algorithm in this study while their collocated CERES footprints are identified as cloudy sky. Mean ± standard deviation of the difference ($OLR_{AIRS\text{-}only}$ – OLR_{CERES}) is also given on the plot.

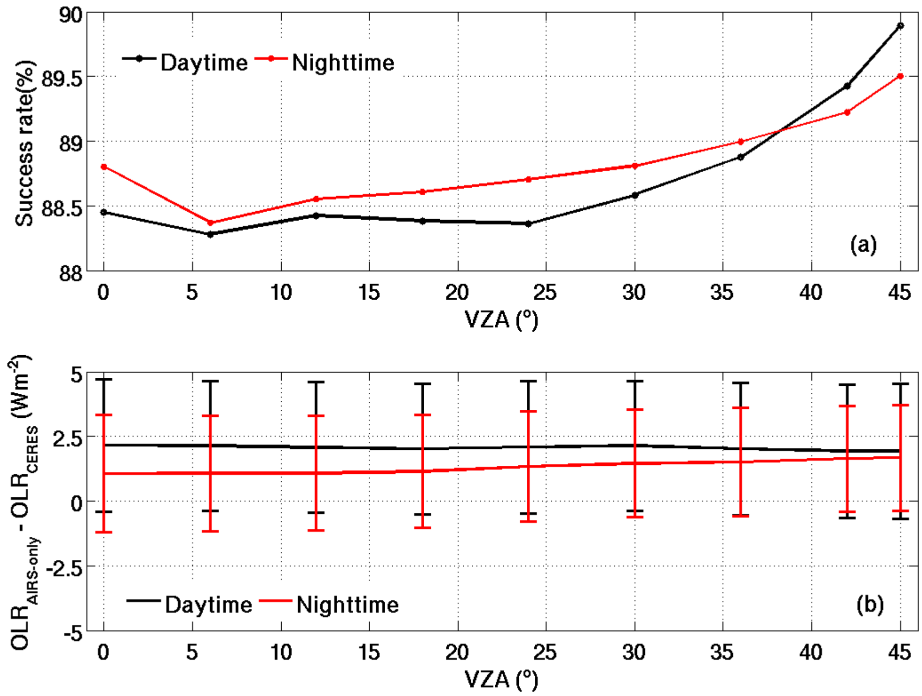

Figure 6. (a) Success rate of the algorithm in distinguishing clear-sky and cloudy-sky footprints as a function of viewing zenith angle (VZA). (b) The difference of $OLR_{AIRS\text{-}only} - OLR_{CERES}$ as a function of VZA. Ticked vertical lines denote the ±1σ (standard deviation).